Research Square

Preprints are preliminary reports that have not undergone peer review.
They should not be considered conclusive, used to inform clinical practice,
or referenced by the media as validated information.

Decoupling strength from refractory attack through Taguchi-guided processing using silica lining in coreless induction melting of Hadfield manganese steel

Lutufyo D. Mwakalukwa
Tanzania Automotive Technology Center – NYUMBU
Richard J. Katemi
rkatemi@gmail.com

University of Dar es Salaam, School of Mines and Geosciences, Department of Mining and Mineral Processing Engineering, P.O. Box 35052
Ngesa E. Mushi
University of Dar es Salaam, College of Engineering and Technology, Department of Mechanical and Industrial Engineering, P.O. Box 35131

Research Article

Keywords: Hadfield manganese steel, silica lining, induction furnace, refractory corrosion, Taguchi method, grey relational analysis

Posted Date: November 18th, 2026

DOI: https://doi.org/10.21203/rs.3.rs-11354135/v1

License: This work is licensed under a Creative Commons Attribution 4.0 International License.
Read Full License

Additional Declarations: No competing interests reported.

Decoupling strength from refractory attack through Taguchi-guided processing using silica lining in coreless induction melting of Hadfield manganese steel

Lutufyo D. Mwakalukwa[1], Richard J. Katemi[2,*], Ngesa E. Mushi[3]

[1] *Tanzania Automotive Technology Center – NYUMBU, Kibaha, Tanzania*

[2] *University of Dar es Salaam, School of Mines and Geosciences, Department of Mining and Mineral Processing Engineering, P.O. Box 35052, Dar es Salaam, Tanzania*

[3] *University of Dar es Salaam, College of Engineering and Technology, Department of Mechanical and Industrial Engineering, P.O. Box 35131, Dar es Salaam, Tanzania*

∗ *Corresponding author. E-mail rkatemi@gmail.com*

ORCID iDs. R.J. Katemi orcid.org/0000-0001-6126-8252, N.E. Mushi orcid.org/0009-0000-5625-186X

Abstract

Silica linings are the cheapest option for coreless induction furnaces but degrade rapidly when Hadfield manganese steel is melted. In the 500 kg furnace studied, a lining that lasts 140–190 heats of cast iron survive only 30–40 heats of manganese steel. The study investigated whether tensile strength and lining attack are governed by different processing variables. A 3^3 full-factorial experimental program (melt temperature 1400–1600 °C, holding time 30–60 min, charge Mn 12–14 wt.%, 27 conditions, 81 heats on one lining) was analyzed by a Taguchi L9 array, S/N ratios, ANOVA, and grey relational analysis, with slag SiO_2 and MnO as indices of lining attack. Manganese content explained 94% of the variation in ultimate tensile strength (UTS), and temperature explained less than 0.1%, whereas temperature explained 80% of the variation in slag SiO_2 and 61% of that in slag MnO. Melting at 1600 °C instead of ≤1500 °C doubled the silica taken up by the slag (19.6 to 40.5 wt.%) with no gain in strength. From nine runs, the Taguchi analysis predicted an optimum of 30 min, 1500 °C and 12 wt.% Mn (1028 MPa), confirmed by three dedicated heats (1029.9 ± 1.5 MPa) and by the factorial run at this condition (1017 MPa), which also ranked first in the multi-response analysis. Under controlled temperature, timed holding, and frequent deslagging, the lining completed 81 heats, about twice the previous lining life. Thus, the charge can set strength, and the thermal schedule can set lining life, offering a low-cost alternative to basic linings.

Keywords: Hadfield manganese steel, silica lining, induction furnace, refractory corrosion, Taguchi method, grey relational analysis

1 Introduction

Austenitic manganese (Hadfield) steel, with about 1.0–1.4 wt.% C and 11–14 wt.% Mn [1], combines high toughness with exceptional work hardening and is the standard material for crusher and mill liners, excavator teeth and railway crossings [2–4]. The as-cast properties of this steel depend mainly on the carbon–manganese balance and on the $(Fe, Mn)_3C$ carbides that form at austenite grain boundaries [5–8], so close control of melt chemistry is essential. In small- and medium-sized foundries, particularly in developing economies, these castings are mostly melted in coreless induction furnaces, which offer fast melting, electromagnetic stirring, and low capital cost [9]. However, refractory crucible wear dominates running costs, as the crucible separates the melt from the water-cooled coil [10,11].

Foundries prefer high-purity quartzite acid linings because basic or neutral linings cost four to six times as much [12], and cast-iron lasts 300–350 heats [13,14]. Silica, however, is chemically incompatible with high-manganese melts. Manganese oxidized at the melt–lining interface fluxes silica into a low-melting manganese-silicate slag that dissolves the hot face, penetrates the open porosity, and releases refractory grains into the steel as inclusions [11,15,16]. Laboratory work has shown how aggressive this attack is. High-Mn steel wets silica-rich refractories at contact angles as low as 10° and erodes them by up to 7.8 mm in a single test [17], thermodynamic modeling

predicts abundant Mn-rich liquid slag when high-Mn steel contacts silica-bearing refractories [18], and even MgO- and spinel-based refractories react with such melts [19–22].

Temperature amplifies the problem. The life of quartzite linings falls from 300–350 to 180–250 heats when the melt temperature rises from about 1450–1500 °C to 1550–1600 °C [12–14], yet Hadfield steel is commonly held at ≥1600 °C to ease deslagging, although the liquidus of the alloy is only about 1370–1400 °C [23]. Overheating also coarsens the austenite grains and increases manganese loss [23–25]. At the Tanzania Automotive Technology Center (TATC–NYUMBU), the same silica lining that gives 140–190 heats with cast iron gives only 30–40 heats with Hadfield steel, forcing frequent, costly relining and raising the risk of metal penetration to the coil.

Previous studies have examined either refractory corrosion in laboratory crucibles [16,17,19] or Hadfield steel properties as a function of composition, melting temperature, or heat treatment [5,24,25], but not both. No study has yet quantified, in an industrial furnace, how melt temperature, holding time, and charge manganese jointly govern lining attack and as-cast strength, so foundries lack an evidence-based processing window. Taguchi orthogonal arrays and grey relational analysis are efficient tools for such multi-factor, multi-response problems [26–30], but refractory engineering has applied them only to formulating refractory materials [31], not to melt–lining compatibility.

The present work hypothesizes that strength, which is set mainly by composition, and lining attack, which arises from thermally activated slag–refractory reactions, are governed by *different* processing factors, so that a temperature–time window exists in which the lining is protected at no cost to strength (Fig. 1). This predicts that (i) UTS is insensitive to melt temperature, (ii) slag indicators of lining attack depend strongly on temperature and time, (iii) the Taguchi optimum for strength coincides with low lining attack, and (iv) operating near this window extends lining life. These predictions are tested with a 3^3 full-factorial experimental program of 81 heats on a single lining, analyzed by Taguchi, ANOVA, and grey relational methods, with the goal of giving silica-lined foundries a practical route to consistent Hadfield steel and longer lining life.

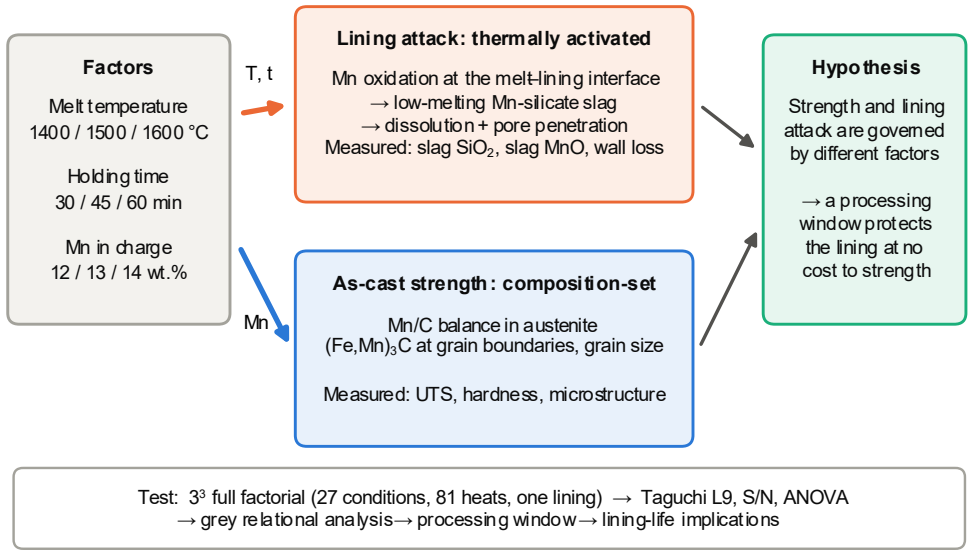


Fig. 1 Conceptual framework. Melt temperature and holding time are expected to drive the thermally activated reactions that attack the silica lining, whereas charge manganese is expected to set the as-cast strength. If the two responses are governed by different factors, a processing window exists that protects the lining without sacrificing strength.

2 Experimental Section

2.1 Materials

The metallic charge consisted of mild-steel scrap, manganese-steel scrap, and manganese-steel foundry returns in the proportions given in Table 1. Before melting, the composition of the incoming manganese-steel scrap was

checked by spark optical emission spectrometry. The scrap contained 1.02–1.12 wt.% C, 0.43–0.47 wt.% Si, 12–14 wt.% Mn, 0.04 wt.% P and 0.02 wt.% S. Ferromanganese (FeMn75) and ferrosilicon (FeSi75) were used to adjust composition, graphite (99% C) as a recarburizer, calcium carbide as a ladle deoxidizer, and Slax 30 (Foseco) as a slag coagulant. The scrap, graphite, ferrosilicon, ramming mix, calcium carbide, Slax 30, and sodium silicate came from Chassl Chemical Group (Ilala, Dar es Salaam), and the ferromanganese and Desulfex-2 (Foseco) came from Namachen Chemical and Industries (Mbagala, Dar es Salaam). The lining was built from a commercial dry silica ramming mix (98.5 wt.% SiO_2) with a boric-acid binder.

Table 1. Base charge proportions for each 500 kg heat.

No.	Charge material	Proportion (wt.%)
1	Mild-steel scrap	60
2	Manganese-steel scrap	20
3	Manganese-steel foundry returns	20
4	Ferromanganese (FeMn75)	As required, Eq. (1)
5	Ferrosilicon (FeSi75)	As required, Eq. (1)

The masses of ferroalloy needed to reach the target composition were calculated from the analysis of the melt with the mass balance

$$m_{alloy} = (\%_{required} - \%_{actual}) \times W_{melt} / \eta_{alloy} \quad (1)$$

where m_{alloy} is the mass of ferroalloy (kg), W_{melt} is the liquid mass (kg), and η_{alloy} is the recovery of the alloying element.

2.2 Furnace and lining construction

All melts were made in a single lining of a 500 kg medium-frequency coreless induction furnace (Inductotherm, USA) at TATC–NYUMBU. The plant followed the ramming procedure (Fig. 2) to install the lining. The water-cooled copper coil was first coated with refractory mortar, dried thoroughly, and then wrapped with thick ceramic (mica) paper to prevent silica from entering the coil. The furnace bottom was rammed in successive layers with spiked and flat-headed tools to about 60 mm thick, and the bottom's flatness was checked with a spirit level. A former made from 4 mm mild-steel plate (Ø230 × 640 mm) was then centered in the coil with wooden spacers and weighted with 100 kg to prevent movement. The 50–60 mm annulus between the former and the ceramic paper was filled and rammed from the bottom upwards, first by hand and finally with pneumatic rammers. A thin layer of sodium silicate solution was applied to the top of the rammed lining, and the tapping mix and spout were then rammed in the same way. Before sintering, the lining was sampled and analyzed by energy-dispersive X-ray fluorescence to establish the initial composition (Table 3).

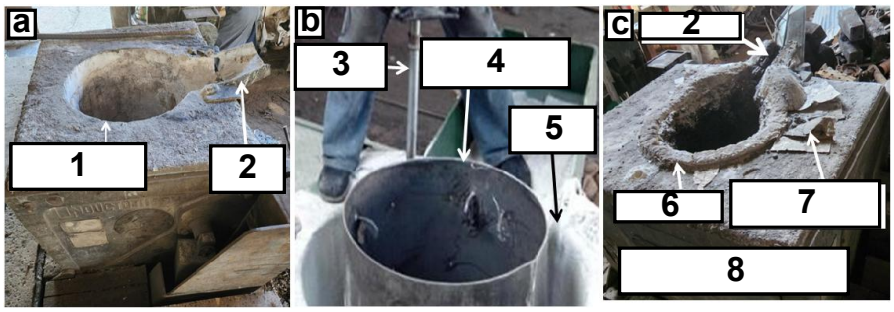


Fig. 2 Construction of the silica lining. (a) Furnace before lining, showing the spout mouth, (b) steel former placed inside the furnace in the ceramic paper, with the ramming hammer, and (c) tapping mix and spout after construction and sintering. Callouts mark (1) the unlined furnace, (2) the spout mouth, (3) the ramming hammer, (4) the former plate, (5) the ceramic paper, (6) the topping mix, (7) ceramic paper pieces after sintering, and (8) the lined furnace with spout after construction and sintering.

The lining was sintered by charging 500 kg of grey cast-iron scrap to the top of the coil. The charge was heated at 100 °C h^{-1} to 800 °C and then at about 150 °C h^{-1} to 1530 °C, held for about 30 min until fully molten, and finally raised to 1600 °C for 1 h to sinter the hot face. Temperatures were read at each step with an immersion thermocouple pyrometer (Keller Cella Port PT) to avoid overstressing the lining. The furnace was then cooled to 1000 °C, and the iron was tapped. After the first (pilot) manganese-steel heat, the lining was inspected for cracks and metal penetration. The sintered crucible measured Ø231 × 643 mm, with a working wall thickness of 10 cm at the thickest section.

2.3 Experimental design and melting program

Three factors were studied, each at three levels (Table 2). Melt temperature and holding time are the two thermal variables that a foundry can control directly. Charge manganese is the compositional variable that sets both the target grade and the manganese activity available for oxidation. Temperature levels span local practice (1600 °C) down to just above the alloy liquidus (1400 °C), and holding times cover the range used for homogenization and deslagging. All $3^3 = 27$ factor combinations were melted, three heats per condition, giving 81 heats on the same lining without any intermediate relining. Each response reported in Table 4 is a single value per condition, obtained from one representative tensile bar and one slag analysis for that condition.

Table 2 Factors and levels.

Factor	Symbol	Level 1	Level 2	Level 3
Holding time (min)	A	30	45	60
Melt temperature (°C)	B	1400	1500	1600
Mn content in charge (wt.%)	C	12	13	14

For each heat, the 500 kg charge was loaded to the maximum possible height, heated at about 150 °C h^{-1} to the set temperature and held isothermally for the set time, with the temperature monitored continuously by immersion pyrometer. During melting, a sample was poured into a 52.4 cm^3 tellurium thermal-analysis cup to determine the carbon equivalent (Supplementary Fig. S1). Carbon was maintained at 1.2–1.4 wt.% in the melt, and manganese was adjusted to the target level using Eq. (1). The slag was skimmed repeatedly during the hold. Immediately before tapping, Slax 30 was sprinkled on the melt to coagulate the remaining slag for collection, minimizing the time the slag spent in contact with the lining [32]. The melt was tapped into a 500 kg mild-steel ladle lined with refractory sand and preheated to 800–1050 °C with oil-fired burners, roughly deoxidized with calcium carbide, and carried by a 3 t overhead crane to the molding area.

Test castings were made in molds of silica sand (AFS fineness 54–70) bonded with 3 wt.% sodium silicate. The sand was mixed for 5–10 min in a sand muller, rammed around wooden (mkanganzi) patterns in 400 × 400 × 100 mm molding boxes, and hardened by gassing with CO_2. The mold cavities were coated with graphite and preheated to 450 °C before pouring. Three casting geometries were produced for each condition, namely Ø25 × 200 mm tensile bars, 100 × 100 × 20 mm blocks for hardness and metallography, and ×50 × 20 mm discs for chemical analysis. The castings solidified in the molds for 24 h before shake-out. Runners, risers, and feeders were then removed by grinding, and the castings were cleaned by shot blasting with 2 mm steel shot. Visual inspection found no shrinkage cavities, blowholes, or surface cracks.

The Taguchi analysis used the standard L9(3^3) orthogonal array [27], made up of the nine combinations of the full factorial marked with † in Table 4. Because all 27 conditions were melted, the conclusions from the L9 could be checked directly against the full factorial. The run at the predicted optimum, which is not part of the L9, served as a first independent check. In addition, three dedicated confirmation heats (C1–C3) were melted at the predicted optimum (30 min, 1500 °C, 12 wt.% Mn) after the factorial program, using the same furnace, charge make-up, melting practice, and deslagging procedure. One tensile bar was cast from each heat and tested in the same way as the factorial specimens.

2.4 Characterization of lining and slag

Slag collected from each condition with a tapping rod (Supplementary Fig. S2) was labeled, cooled, crushed to powder in a pan, and analyzed for SiO_2 and MnO with an energy-dispersive X-ray fluorescence spectrometer (EDX-800 series) at the Tanzania Bureau of Standards (Supplementary Fig. S3). Lining samples were taken before the first heat and after the 81st heat and analyzed in the same way. The residual wall thickness at the most eroded section was measured after the 81st heat, and sections of the spent lining were examined visually for slag penetration. Because the EDX analyses were semi-quantitative and covered only SiO_2 and MnO in the slag, the results are interpreted as relative indices of lining dissolution and manganese oxidation, not as complete slag analyses.

2.5 Characterization of cast steel

The chemical composition of each cast disc was measured by spark optical emission spectrometry (Bruker Q8 Columbus, argon purge at 3 bars, tungsten counter-electrode). Each ground sample was sparked at least twice at different positions to check reproducibility, and the results were compared with ASTM A128 [1]. Tensile tests were carried out to ASTM A370 [33] on a 200 t hydraulic universal testing machine (model DMU) with load and strain control, at a constant loading rate of 11.5 MPa s^{-1}. The bars were tested in the as-cast condition without machining to a standard gauge diameter, so the results are for comparison between conditions rather than for design. This work analyzes ultimate tensile strength (UTS), the maximum engineering stress before fracture. Brinell hardness was measured per ASTM E10 [34] on a Future Tech FB-3000 tester using a 10 mm ball and a 3000 kgf load on smooth, scale-free surfaces of the hardness blocks.

For metallography, 25 mm square sections were cut from the hardness blocks with an abrasive cut-off wheel and ground with SiC papers (grit 200, 320, 400, 600, and 1200), using lubricant for the coarser grades. They were then polished with 0.05 μm Al_2O_3 suspension to a mirror finish, etched in 2% Nital for about 30 s, rinsed in alcohol, and dried in warm air (Supplementary Fig. S4). The microstructures were examined with a binocular metallurgical microscope (BS 6025 TRF, 50–1000×) and compared with standard reference charts for manganese steel at the same magnification.

Because the original specimens were no longer available, the archived micrographs, one representative field per condition at a nominal magnification of 100×, were analyzed by image analysis following the principles of ASTM E1245 [35]. Annotations added to the images (arrows and labels) and an 8-pixel border were masked. Each image was converted to the CIELAB color space, and every pixel was compared with the local matrix background obtained by a 41-pixel median filter, which compensates for uneven etching and illumination. Grain-boundary carbide colonies were identified as regions brighter than the local matrix by more than 8 L∗ units or with a chroma below 62% of the local matrix value. These regions were merged by a morphological closing and retained when larger than 40 pixels. A second, more inclusive criterion that also accepted strongly textured regions gave an upper estimate, so each carbide fraction is reported as a range. Dark particles were defined as compact features darker than the local matrix by more than 18 L∗ units that survived a morphological opening, which removes the thin grain-boundary lines. All quantities are area fractions or counts per field and therefore do not depend on the absolute magnification calibration. The segmentation masks are given in Supplementary Fig. S5.

2.6 Statistical analysis

The S/N ratios were calculated for the larger-the-better characteristic (UTS) and for the smaller-the-better characteristics (slag SiO_2 and MnO) as follows [26].

$$\eta_{LB} = -10\, log_{10}[(1/n)\, \Sigma\, (1/y_i^2)], \quad \eta_{SB} = -10\, log_{10}[(1/n)\, \Sigma\, y_i^2] \tag{2}$$

where y_i is the measured response and n is the number of observations per run. With one value per run, Eq. (2) reduces to $\eta_{LB} = +20 \log_{10} y$ and $\eta_{SB} = -20 \log_{10} y$. ANOVA partitioned the total sum of squares among the factor effects. For the L9 array, the three factors used six degrees of freedom and the remaining two formed the error term [36]. For the full factorial, the three main effects and the three two-factor interactions were estimated, and the three-factor interaction (eight degrees of freedom) was pooled as error [37]. The percentage contribution of each source was taken as $SS_{source}/SS_{total} \times 100$. The use of one value per condition follows standard practice for unreplicated factorial and orthogonal-array experiments, in which the experimental error is estimated from the

pooled highest-order interaction instead of from repeated runs [27,37]. This approach is justified here on four grounds. First, the full factorial contains hidden replication, because each factor-level mean is the average of nine different conditions and each main effect is estimated from all 27 conditions. Second, the pooled error term was small, accounting for only 0.14% of the total variance in UTS (standard deviation of about 6 MPa), so the dominant effects exceed the error by two to three orders of magnitude in F-value. Third, any significant interaction would inflate rather than reduce the pooled error, which makes the significance tests conservative. Fourth, reproducibility was verified directly by three dedicated confirmation heats at the optimum, whose UTS varied by a coefficient of variation of only 0.14% (Table 9). The response at the optimum was predicted with the additive model

$$\hat{y}_{opt} = \bar{y} + (\bar{y}_A - \bar{y}) + (\bar{y}_B - \bar{y}) + (\bar{y}_C - \bar{y}) \quad (3)$$

where $\bar{y}$ is the grand mean and $\bar{y}_A$, $\bar{y}_B$ and $\bar{y}_C$ are the mean responses at the optimal levels of the three factors. The 95% confidence interval of the prediction was $CI = [F_{0.05,1,ve}\ V_e\ (1/n_{eff} + 1/r)]^{1/2}$, where V_e is the error variance with ν_e degrees of freedom, $n_{eff} = N/(1 +$ total degrees of freedom of the factors) and r is the number of confirmation tests [27]. For multi-response optimization, each response was normalized to the range 0–1, with UTS treated as larger-the-better and slag SiO_2 and MnO as smaller-the-better. The grey relational coefficients were then calculated with a distinguishing coefficient $\zeta = 0.5$ and averaged with equal weights to give the grey relational grade (GRG) of each condition [29,30].

3 Results and Discussion

The results are presented from the furnace downwards, following the hypothesis in Fig. 1. The degradation of the lining over the 81-heat service period is established first, together with the response of slag chemistry, as an index of that degradation, to the processing variables. The composition, strength, hardness and microstructure of the steel are then examined, and the two sets of responses are shown to be governed by different factors. Finally, Taguchi and multi-response analyses identify and validate the processing window, and the implications for lining life are discussed.

3.1 Degradation of the silica lining service life

The lining completed all 81 heats of Hadfield steel without relining, about twice the 30–40 heats normally achieved at TATC (Fig. 3a). The lining composition before and after the 81-heat service period (Table 3, Fig. 3b) shows what happened at the hot face. The SiO_2 content fell from 98.10 to 94.26 wt.%, while MnO rose 31-fold (from 0.053 to 1.656 wt.%) and Fe_2O_3 rose nine-fold (from 0.082 to 0.728 wt.%). The contents of B_2O_3 (the binder) and K_2O did not change. The selective uptake of manganese and iron oxides, with no binder loss, indicates that the lining degraded mainly by reaction with oxides from the melt and slag rather than by mechanical abrasion. At the most eroded section, the working wall thinned from 10 to 4 cm, an average of about 0.74 mm per heat over the service period.

Table 3 Chemical composition (wt.%, EDX) and wall thickness of the silica lining before the first heat and after the 81st heat.

Constituent	Before first heat	After 81 heats	Change
SiO_2	98.10	94.26	−3.84
MnO	0.053	1.656	+1.603
Fe_2O_3	0.082	0.728	+0.646
B_2O_3	1.20	1.20	0
K_2O	0.72	0.72	0
Other oxides	0.565	0.14	−0.425
Wall thickness, most eroded section (cm)	10	4	−60%

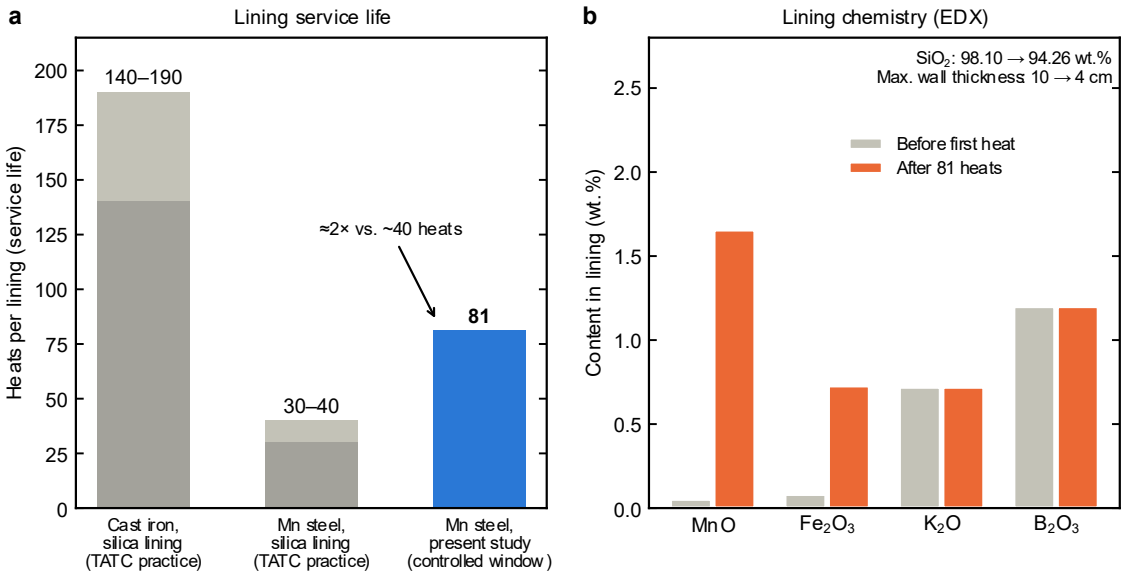


Fig. 3 (a) Service life of the silica lining for cast iron and Hadfield steel under previous TATC practice, compared with the present study (grey shading shows the plant range). (b) Minor-oxide content of the lining before and after 81 heats. The inset shows the SiO_2 content and wall thickness.

Sections cut from the spent lining show how the attack progressed (Fig. 4). A dark, glassy slag layer adheres to the hot face, and slag has penetrated up to about 2 cm into the lining along pores and grain boundaries between the quartz aggregates. This morphology matches the dissolution–penetration mechanism reported for silica refractories in induction furnaces [16] and for oxide refractories in general [10]. At the interface, oxygen from the furnace atmosphere and the lining porosity oxidizes manganese in the melt (Eq. 4), and manganese can also reduce silica directly, transferring silicon to the steel (Eq. 5) [15,18]. The basic MnO then combines with the acidic silica to form manganese silicates (rhodonite, $MnSiO_3$, and tephroite, Mn_2SiO_4) whose liquidus, roughly 1250–1350 °C, lies well below the operating temperature (Eq. 6) [15].

$$[Mn] + [O] \rightarrow (MnO) \tag{4}$$

$$2[Mn] + SiO_2(s) \rightarrow 2(MnO) + [Si] \tag{5}$$

$$x(MnO) + SiO_2(s) \rightarrow (xMnO \cdot SiO_2)(l) \tag{6}$$

The liquid silicate dissolves the fine matrix and binder phase and infiltrates the open porosity left after sintering. The infiltrated zone loses strength, and coarse quartz grains are released into the melt as potential exogenous inclusions [11]. Because penetration is driven by slag fluidity and slag–lining contact time, penetration should depend strongly on temperature and holding time, which is examined next through the chemistry of the slag.

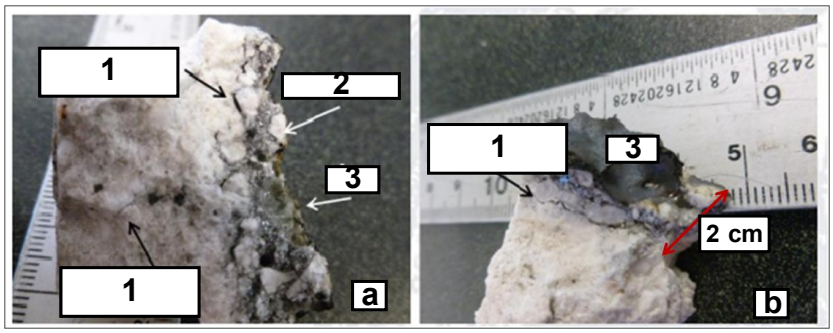
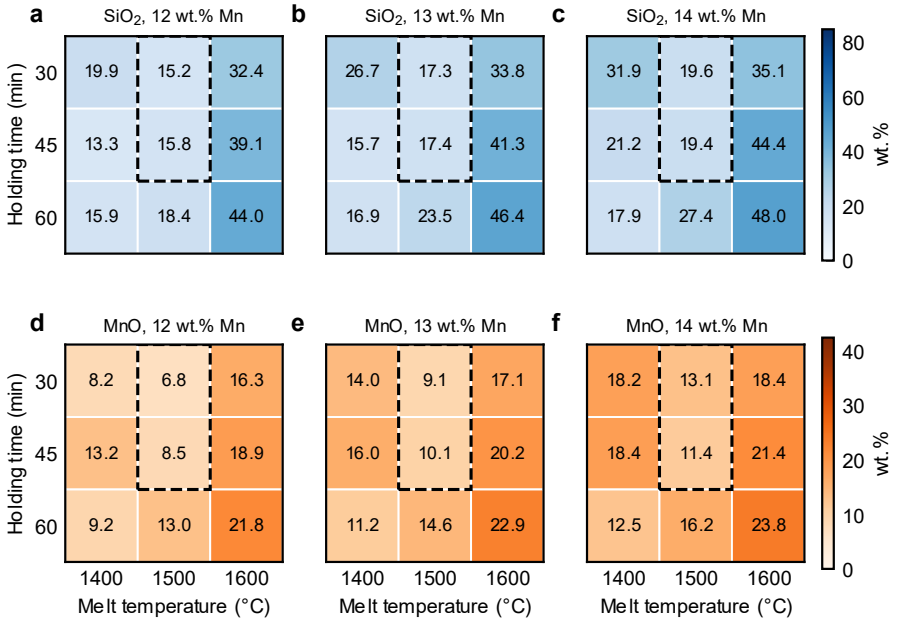


Fig. 4 Sections of the silica lining after 81 heats. (a) Slag penetrating along pores and grain boundaries between quartz aggregates and (b) slag layer at the hot face, with penetration of about 2 cm. Callouts mark (1) slag penetrated into the lining, (2) the refractory, and (3) the slag.

3.2 Lining attack index

After cooling, the slag was vitreous and dark grey, with black residues attributed to the graphite recarburizer, and the slag from 1600 °C contained a whitish, powdery fraction (Supplementary Fig. S2b). Apart from minor oxidation of the silicon in the charge (0.43–0.51 wt.% Si), the lining is the only significant source of SiO_2 in the system. Therefore, the SiO_2 content of the slag is used as an index of lining dissolution, and the MnO content as an index of manganese oxidation. Across the 27 conditions, the two were strongly correlated (r = 0.89), consistent with their co-production as manganese silicate (Eq. 6) [15]. Fig. 5 maps both oxides over the full factorial, and Table 5 gives the ANOVA. Melt temperature had the largest effect. At 1600 °C, the slag contained 32–48 wt.% SiO_2 (mean 40.5 wt.%), against 13–32 wt.% (mean 19.6 wt.%) at 1400–1500 °C. Temperature alone explained 79.8% of the variance in slag SiO_2 and 61.2% in slag MnO (both $p < 0.001$). Charge manganese moderately increased both oxides, accounting for 4.4% of the variance in SiO_2 and 12.9% in MnO, as expected from the higher activity of manganese available for Eqs. (4) and (5).



Dashed box: 1500 °C / 30–45 min processing window.

Fig. 5 Content of (a–c) SiO_2 and (d–f) MnO in the slag at 12, 13 and 14 wt.% Mn for every combination of melt temperature, holding time, and charge Mn (27 conditions). The dashed box marks the 1500 °C / 30–45 min window, in which both oxides are lowest at every Mn level.

Holding time mattered mainly through its interaction with temperature, explaining 12.5% of the variance in SiO_2 and 15.6% in MnO ($p < 0.001$). At 1600 °C, slag SiO_2 (averaged over the three Mn levels) rose steadily with holding time, from 33.8 to 41.6 and 46.1 wt.% at 30, 45, and 60 min, and slag MnO rose from 17.3 to 20.2 and 22.9 wt.%. At 1500 °C, by contrast, slag SiO_2 stayed at 17–18 wt.% up to 45 min and rose only after 60 min (23.1 wt.%). In other words, the lining tolerates longer holds at 1500 °C, but at 1600 °C every additional minute of contact measurably increases attack. Prolonged high-temperature holding is therefore doubly harmful, with direct consequences for practice.

The strong temperature dependence agrees with industrial experience with quartzite linings, whose durability falls by up to about half when the melt temperature rises from about 1450–1500 °C to 1550–1600 °C [12–14]. This trend also matches the severe erosion of silica-rich refractories by high-Mn steel in laboratory tests [17]. At least three mechanisms act together above 1500 °C. First, silica dissolves faster in MnO-bearing silicate slag, so the rate of Eq. (6) increases [15]. Second, the slag becomes less viscous and wets the lining more readily, so the slag penetrates the pores faster and deeper [10,17]. Third, carbothermic reduction of silica becomes significant in a carbon-saturated melt, providing an additional route for silica loss (Eq. 7) [32].

$$SiO_2(s) + 2[C] \rightarrow [Si] + 2CO(g) \quad (7)$$

The small but systematic rise in the silicon content of the steel at 1600 °C (mean 0.466 wt.%, against 0.447 wt.% at 1400 °C and 0.450 wt.% at 1500 °C) supports the transfer of silicon from the lining to the melt through Eqs. (5) and (7).

Slag MnO was also somewhat higher at 1400 °C than at 1500 °C (13.5 vs. 11.4 wt.% on average), so the temperature-attack relationship is not simply monotonic at the low end. At 1400 °C, the melt is only about 30 °C above the liquidus [23]. Melting is slow, and the slag is viscous, so Mn-rich slag may stay on the wall longer and be removed less completely during skimming. The steel's manganese balance supports this interpretation. The largest Mn loss occurred at 1400 °C (0.30 wt.% on average, and 0.99 wt.% at 30 min/12 wt.% Mn). At 1500 °C, Mn was almost fully recovered (mean loss 0.07 wt.%). At 1600 °C, the cast Mn was slightly above the charge target (mean +0.12 wt.%), as expected when carbothermic reduction of MnO, (MnO) + [C] → [Mn] + CO(g), becomes favorable at higher temperatures [15]. A melt temperature of about 1500 °C thus combines efficient melting with minimal manganese oxidation and minimal silica dissolution.

3.3 Physicochemical properties of the cast steel

The composition of all 27 casts stayed within narrow limits (Table 4). Carbon ranged from 1.01 to 1.12 wt.%, silicon from 0.43 to 0.51 wt.%, and phosphorus was 0.04 wt.% throughout. Manganese ranged from 11.01 to 14.08 wt.% and was within ±0.35 wt.% of the charge target in all but two casts, both melted at 1400 °C for 30 min (−0.99 and −0.74 wt.%). The spread in manganese was therefore much smaller than the 1 wt.% steps between the factor levels, so the charge Mn level is a valid proxy for the Mn content of the cast. Although lining attack was clearly visible in the slag and lining, the attack did not measurably contaminate the steel. Silicon content varied by 0.08 wt.%, and the castings showed no visible defects.

Table 4. Results of the full 3^3 factorial experimental program. Rows marked † form the Taguchi L9 array and ‡ marks the predicted optimum, which is not part of the L9.

Time (min)	Temp. (°C)	Mn charge (wt.%)	UTS (MPa)	Slag SiO_2 (wt.%)	Slag MnO (wt.%)	Mn cast (wt.%)	Si cast (wt.%)	HB	GRG
30†	1400	12	1021	19.87	8.21	11.01	0.44	220	0.863
30‡	1500	12	1017	15.15	6.84	12.06	0.45	191	0.959
30	1600	12	1020	32.40	16.30	12.20	0.44	223	0.647
30	1400	13	981	26.67	13.96	12.26	0.45	227	0.625
30†	1500	13	989	17.34	9.11	13.21	0.46	220	0.802
30	1600	13	995	33.80	17.10	13.10	0.46	209	0.582
30	1400	14	802	31.87	18.21	13.91	0.45	230	0.428
30	1500	14	812	19.56	13.09	14.08	0.46	220	0.566
30†	1600	14	820	35.12	18.40	14.06	0.47	202	0.420
45	1400	12	972	13.35	13.24	11.79	0.43	193	0.766
45	1500	12	988	15.83	8.46	11.94	0.44	220	0.838
45†	1600	12	990	39.15	18.92	12.30	0.44	194	0.541
45†	1400	13	962	15.66	16.01	12.86	0.44	198	0.684
45	1500	13	971	17.41	10.10	12.96	0.44	200	0.752
45	1600	13	978	41.30	20.21	13.20	0.46	188	0.508
45	1400	14	786	21.23	18.45	13.82	0.45	200	0.489
45†	1500	14	803	19.36	11.40	13.99	0.45	191	0.589
45	1600	14	801	44.36	21.40	14.00	0.48	187	0.366
60	1400	12	1009	15.86	9.21	11.89	0.44	171	0.857
60†	1500	12	980	18.43	13.00	11.71	0.44	169	0.705
60	1600	12	981	44.02	21.80	12.10	0.46	161	0.496
60	1400	13	920	16.94	11.21	12.85	0.45	170	0.684
60	1500	13	926	23.47	14.60	12.65	0.45	171	0.578
60†	1600	13	920	46.36	22.92	13.05	0.47	188	0.418
60†	1400	14	779	17.86	12.54	13.93	0.47	175	0.581
60	1500	14	760	27.38	16.20	13.79	0.46	168	0.454
60	1600	14	762	47.98	23.84	14.06	0.51	158	0.334

UTS ranged from 760 to 1021 MPa and fell into three distinct bands set by manganese content, namely, 972–1021 MPa at 12 wt.%, 920–995 MPa at 13 wt.% and 760–820 MPa at 14 wt.% (Table 4). In the full-factorial ANOVA (Table 5), manganese content explained 94.0% of the variance in UTS and holding time 4.3% (both $p < 0.001$),

with a small time × Mn interaction (1.1%, $p < 0.001$). Melt temperature explained only 0.03% ($p = 0.45$). The mean UTS was 918.6 MPa for heats melted at 1600 °C and 915.4 MPa for heats melted at 1400–1500 °C, a difference far smaller than the experimental error. Prediction (i) is therefore confirmed. Over 1400–1600 °C, temperature, the variable that controls lining attack, has no measurable effect on the strength of the as-cast steel. The modest decline in UTS with holding time (mean 939.7, 916.8 and 893.0 MPa at 30, 45 and 60 min) may reflect the progressive loss of heterogeneous nuclei, such as fine oxide particles, during prolonged holding of the melt, which favors a coarser as-cast structure, but the present data do not allow this mechanism to be confirmed.

Table 5 Full-factorial ANOVA giving the percentage contribution and p-value for each source (27 conditions, three-factor interaction pooled as error with 8 degrees of freedom).

Source	DF	UTS %	UTS p	Slag SiO_2 %	SiO_2 p	Slag MnO %	MnO p
Holding time (A)	2	4.25	<0.001	1.88	0.017	5.62	<0.001
Temperature (B)	2	0.03	0.449	79.84	<0.001	61.20	<0.001
Mn content (C)	2	93.98	<0.001	4.35	0.001	12.93	<0.001
A × B	4	0.43	0.014	12.52	<0.001	15.61	<0.001
A × C	4	1.09	<0.001	0.09	0.946	1.48	0.117
B × C	4	0.08	0.380	0.26	0.746	2.03	0.060
Error (A × B × C)	8	0.14	–	1.06	–	1.14	–
Total	26	100		100		100	

Fig. 6 shows representative as-cast microstructures for the nine combinations of manganese content and melt temperature, and Table 6 summarizes the image-analysis results. All specimens consist of an austenitic matrix with three morphological types of second-phase features. Type 1 features are fine, discontinuous precipitates and thin films that outline the austenite grain boundaries and dominate at 1400 °C (Fig. 6a, d, g). Type 2 features are semi-continuous grain-boundary networks in which light-etching carbide is mixed with darker constituents, most evident at 1500 °C and in the 12 wt.% Mn steel melted at 1600 °C (Fig. 6c, e). Type 3 features are coarse colonies of light-yellow lamellar and globular carbide at grain-boundary junctions, observed only at 1600 °C and most extensive at 13 wt.% Mn (Fig. 6f, i). Lamellar, pearlite-like carbide colonies characterize Hadfield steel that cools slowly through the carbide precipitation range, as in sand molds and thicker sections [2,4].

The dark, near-equiaxed particles visible in several fields, most numerous at 12 wt.% Mn and 1400 °C (Fig. 6a), are interpreted as micropores and non-metallic inclusions. An earlier description of these features as graphite [38] is not retained, because graphite is not expected in an Fe–1C–12Mn steel, in which manganese strongly stabilizes cementite-type carbides and suppresses graphitization [2]. At 1400 °C, where these particles are most numerous, their median minor-to-major axis ratio is 0.7–0.9 (Table 6), a near-equiaxed shape consistent with gas pores or globular oxide and sulfide inclusions. Unambiguous identification would require SEM/EDS, which could not be performed on the archived material.

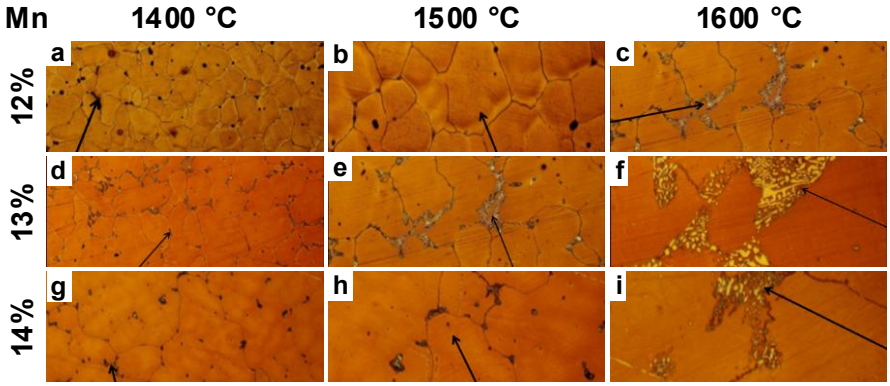


Fig. 6 Representative as-cast microstructures (optical, 2% Nital, nominal magnification 100×) for charge Mn contents of 12, 13 and 14 wt.% (rows) and melt temperatures of 1400, 1500 and 1600 °C (columns). Arrows mark a dark particle interpreted as a pore or inclusion (a), austenite grain boundaries with thin carbide films (b, d, g, h), semi-continuous carbide networks (c, e), and lamellar carbide colonies (f, i).

Table 6. Semi-quantitative image analysis of the archived micrographs (one field per condition). The carbide colony fraction is the range between the conservative and inclusive segmentation criteria.

Mn (wt.%)	Temp. (°C)	Dominant carbide type	Carbide colony fraction (%)	Dark-particle area (%)	Dark particles per field	Median axis ratio of particles
12	1400	1	0.3–1.5	1.28	34	0.88
12	1500	1–2	1.5–1.8	0.78	15	0.79
12	1600	2	2.0–2.2	0.28	6	0.68
13	1400	1	0.2–0.4	0.05	2	–
13	1500	2	1.7–2.0	0.30	6	0.68
13	1600	3	13.5–16.3	0.02	1	–
14	1400	1	0.2–0.4	0.40	10	0.70
14	1500	1	0.2–0.4	1.21	15	0.56
14	1600	3	1.3–1.8	0.13	3	0.53

Image analysis confirms a clear effect of melt temperature on grain-boundary carbide. The carbide colony fraction rose from 0.2–1.5% at 1400 °C to 0.2–2.0% at 1500 °C and 1.3–16% at 1600 °C, with the highest value corresponding to the lamellar colonies at 13 wt.% Mn (Table 6). The austenite grains also appeared coarser at 1500 and 1600 °C than at 1400 °C, in line with reports that higher melting and casting temperatures coarsen the as-cast austenite of Hadfield steel [23,24]. Dark particles followed the opposite trend. Their area fraction averaged 0.6% at 1400 °C and 0.8% at 1500 °C but only 0.1% at 1600 °C, and their number per field decreased accordingly. The melt's lower viscosity at higher superheat favors inclusion flotation and gas escape, which may explain this trend. The more intense attack on the lining at 1600 °C therefore did not produce a higher content of exogenous particles in the castings, consistent with the narrow range of silicon content in the steel (Table 4).

These microstructural trends must be reconciled with the tensile data. Melt temperature markedly changed the carbide colony fraction and grain size, yet had no measurable effect on UTS. The condition with the most extensive lamellar colonies (13 wt.% Mn, 1600 °C) had a UTS (920–995 MPa over the three holding times) that did not differ from that at 1400 °C (920–981 MPa). Within the range studied, therefore, the amount of grain-boundary carbide revealed by optical microscopy does not control the as-cast tensile strength. Manganese content does. A plausible explanation lies in the austenite's deformation behavior. At a nearly constant carbon content of

about 1.05 wt.%, increasing manganese moves the Mn/C ratio away from the conventional 10 to 1 balance of Hadfield steel [2] and alters the stacking fault energy of the austenite, which governs the balance between deformation twinning and dislocation glide and hence the strain hardening that sustains the tensile load up to fracture [39,40]. Confirming this mechanism requires examining the deformed microstructure, so the microstructural conclusions drawn here from one archived field per condition are semi-quantitative.

Brinell hardness ranged from 158 to 230 HB, typical of as-cast, unhardened Hadfield steel. Unlike UTS, hardness depended mainly on holding time (78% of the variance), with means of 216, 197, and 170 HB at 30, 45, and 60 min, respectively ($p < 0.001$). Neither manganese content nor melt temperature had a significant effect. The fall in hardness with longer holds parallels the fall in UTS, and both trends are consistent with a coarser as-cast structure after prolonged holding, although grain size could not be measured for every holding time. Short holds therefore favor both strength and hardness, which is consistent with what the lining requires.

3.4 Strength and lining attack governing factors

Figs. Figs. 7 and 8 bring these results together and show the central finding of this work. The factor that dominates strength, manganese content (94% of the variance in UTS), contributes little to lining attack (4% of the variance in slag SiO_2). The factor that dominates lining attack, melt temperature (80% of slag SiO_2 and 61% of slag MnO), contributes essentially nothing to strength (0.03%). Holding time plays a secondary role in both, mainly through the interaction with temperature on the lining side. Prediction (ii) is confirmed, and the hypothesis that the two responses are decoupled is supported by the full data set.

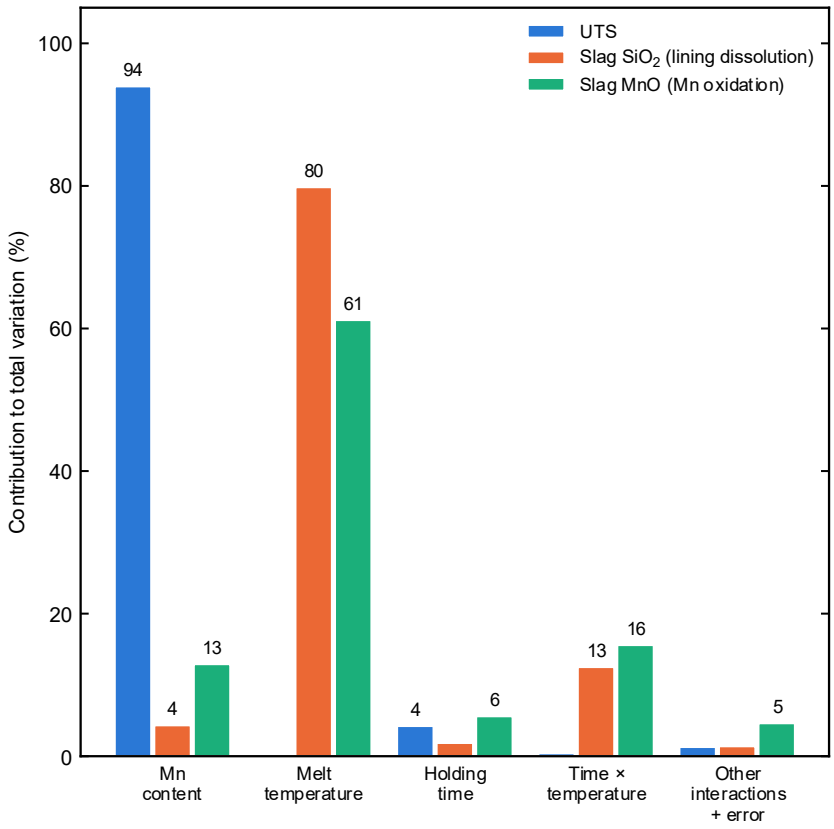


Fig. 7 Percentage contribution of each factor to the variation in UTS, slag SiO_2 (lining dissolution), and slag MnO (Mn oxidation), from the full-factorial ANOVA. Different factors govern strength and lining attack.

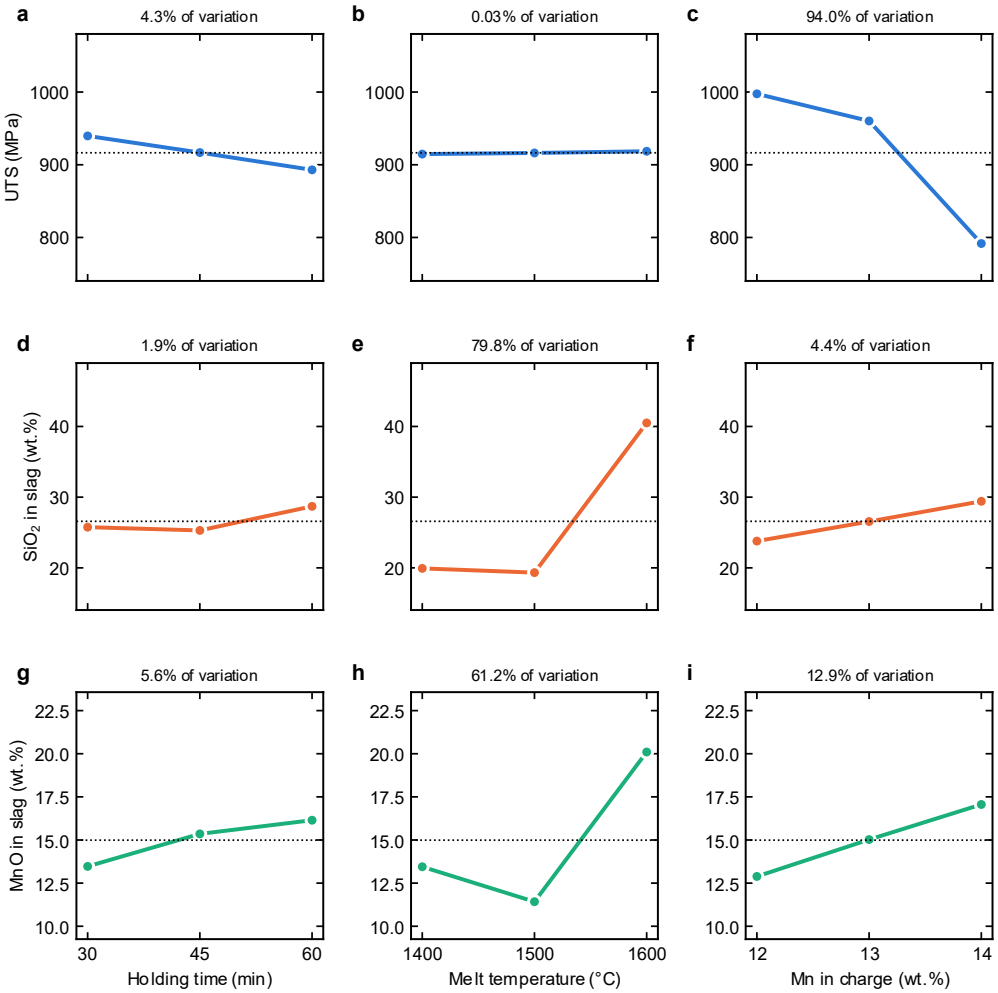


Fig. 8 Main-effect plots (means over the 27 conditions) of holding time, melt temperature and charge Mn for (a–c) UTS, (d–f) slag SiO_2, and (g–i) slag MnO. Each panel gives the percentage contribution of the factor. The dotted line is the grand mean.

The practical significance of this decoupling is that the two production targets can be met by adjusting different factors independently. Strength is secured by keeping manganese at the low end of the specification (about 12 wt.%) at fixed carbon. Lining protection is secured through the thermal schedule, by melting at about 1500 °C instead of 1600 °C and limiting the hold to 30–45 min. Neither adjustment compromises the other. Melting at 1600 °C has the opposite effect, doubling the silica taken up by the slag and raising slag MnO by 62%, with no measurable gain in strength. For a foundry, this is the most direct and least expensive change available, requiring no new materials or equipment, only tighter temperature control.

3.5 Taguchi optimization and validation of strength

With the dominant factors established, the next question was whether a Taguchi design, which requires only nine of the 27 conditions, would reach the same conclusions and identify the correct optimum. The L9 response table (Table 7) ranks the factors by their effect on UTS as manganese content (range of level means Δ = 196.3 MPa, S/N Δ = 1.91 dB), then holding time (50.3 MPa, 0.48 dB), and then melt temperature (14.0 MPa, 0.12 dB). The highest mean S/N ratios occur at 30 min, 1500 °C, and 12 wt.% Mn (Fig. 9a–c). The L9 ANOVA (Table 8) gives contributions of 93.92% for Mn ($p = 0.0009$), 5.53% for time ($p = 0.015$), and 0.47% for temperature ($p = 0.16$, not significant), with an error of only 0.09%. These values closely match the full-factorial contributions (94.0%, 4.3%, and 0.03%, Table 5). With a third of the experimental effort, the orthogonal array therefore recovered the

correct ranking and significance of the factors. This illustrates the economy of Taguchi designs for problems governed mainly by main effects with a single response [27,28].

Table 7. Taguchi L9 response table giving the mean UTS (MPa) and mean S/N ratio (dB, larger-the-better) at each factor level. Bold values mark the optimum level.

Level	Time, UTS	Time, S/N	Temp., UTS	Temp., S/N	Mn, UTS	Mn, S/N
Level 1	**943.33**	**59.454**	920.67	59.225	**997.00**	**59.973**
Level 2	918.33	59.224	**924.00**	**59.274**	957.00	59.614
Level 3	893.00	58.977	910.00	59.155	800.67	58.067
Δ (max − min)	50.33	0.477	14.00	0.119	196.33	1.905
Rank	2	2	3	3	1	1

Table 8. ANOVA of UTS for the L9 array.

Source	DF	SS	MS	F	p	Contribution (%)
Holding time	2	3800.22	1900.11	63.81	0.0154	5.53
Temperature	2	320.89	160.44	5.39	0.1565	0.47
Mn content	2	64586.89	32293.44	1084.48	0.0009	93.92
Error	2	59.56	29.78	–	–	0.09
Total	8	68767.56				100.00

From Eq. (3), the predicted UTS at the optimum is $\hat{y}_{opt}$ = 918.22 + (943.33 − 918.22) + (924.00 − 918.22) + (997.00 − 918.22) = 1027.9 MPa. The optimal combination is not one of the nine L9 runs, but this condition was melted as part of the full factorial and so provides a genuinely independent check. The measured UTS was 1017 MPa, 1.06% below the prediction and well within the 95% confidence interval of ±31.3 MPa ($F_{0.05,1,2}$ = 18.51, V_e = 29.78 MPa^2, n_{eff} = 1.29, r = 1) (Table 9). The three dedicated confirmation heats gave 1031.60, 1029.22 and 1028.87 MPa (mean 1029.90 ± 1.49 MPa, coefficient of variation 0.14%), only 0.19% above the prediction and well within the corresponding 95% confidence interval of ±24.7 MPa for r = 3 (Table 9). The difference of about 13 MPa between the confirmation mean and the factorial run lies within both confidence intervals and is of the same order as the heat-to-heat scatter in the factorial data (error standard deviation of about 6 MPa in the full-factorial ANOVA). Both independent checks therefore show that the additive model predicts the strength reliably and that the optimum identified from nine runs is reproducible.

Table 9 Prediction and confirmation of UTS at the optimum (30 min, 1500 °C, 12 wt.% Mn).

Basis	n	UTS (MPa)	Deviation from prediction	95% CI
Taguchi prediction from L9, Eq. (3)	–	1027.9	–	–
Full-factorial run (independent of L9)	1	1017	−1.06%	±31.3 MPa ✓
Dedicated confirmation heats C1, C2 and C3 (1031.60, 1029.22 and 1028.87 MPa)	3	1029.90 ± 1.49	+0.19%	±24.7 MPa ✓

The comparison also shows where the Taguchi approach reaches a limit. With only nine runs and all degrees of freedom used by the main effects, the L9 cannot estimate interactions. For UTS, this does not matter, since all interactions together contribute only 1.6% of the variance. For the lining responses, however, the time × temperature interaction contributes 12.5–15.6% (Table 5). The full factorial was needed to show that long holds

are harmful mainly at 1600 °C. Orthogonal arrays are therefore efficient for screening and for optimizing strength, but where thermally activated refractory reactions are involved, designs that can resolve interactions, such as full or higher-resolution fractional factorials, are advisable [37].

3.6 Multi-response optimum for strength and lining protection

A single-response optimum alone cannot show that strength is achieved without harming the lining. To optimize both together, UTS (larger-the-better), slag SiO_2 and slag MnO (both smaller-the-better) were combined into a single grey relational grade. Over all 27 conditions, the highest GRG was obtained at 30 min, 1500 °C and 12 wt.% Mn (GRG = 0.959, Table 10), exactly the Taguchi optimum for strength. Prediction (iii) is therefore confirmed. Under these conditions, the UTS was 1017 MPa (second highest of 27), the slag MnO was 6.84 wt.% (lowest of 27), and the slag SiO_2 was 15.15 wt.% (second lowest). The next-ranked conditions also share low manganese and temperatures of 1400–1500 °C, whereas eight of the nine conditions at 1600 °C rank in the lower half (Table 4).

Table 10. The five highest-ranked conditions by grey relational grade (UTS, slag SiO_2, and slag MnO equally weighted, 27 conditions).

Rank	Time (min)	Temp. (°C)	Mn (wt.%)	UTS (MPa)	Slag SiO_2 (wt.%)	Slag MnO (wt.%)	GRG
1	30	1500	12	1017	15.15	6.84	0.959
2	30	1400	12	1021	19.87	8.21	0.863
3	60	1400	12	1009	15.86	9.21	0.857
4	45	1500	12	988	15.83	8.46	0.838
5	30	1500	13	989	17.34	9.11	0.802

The factor-level GRG means lead to the same conclusion (Fig. 9d–f). Both the L9 subset and the full factorial favor 30 min and 12 wt.% Mn, and both penalize 1600 °C heavily (GRG 0.450 in the L9 and 0.479 in the full factorial). In the L9, 1400 and 1500 °C score almost equally (0.753 and 0.738), and the full data resolve the choice in favor of 1500 °C (0.693 against 0.664), reflecting the lower slag MnO (Fig. 5) and better Mn recovery (Table 4) at that temperature. Taken together, the single- and multi-response analyses define a robust processing window with a melt temperature of about 1500 °C, a hold of 30–45 min, and manganese at the low end of the grade (12–13 wt.%), outlined by the dashed box in Fig. 5. Within this window, at 12–13 wt.% Mn, the slag SiO_2 stayed at 15–18 wt.% and the UTS at 970–1020 MPa.

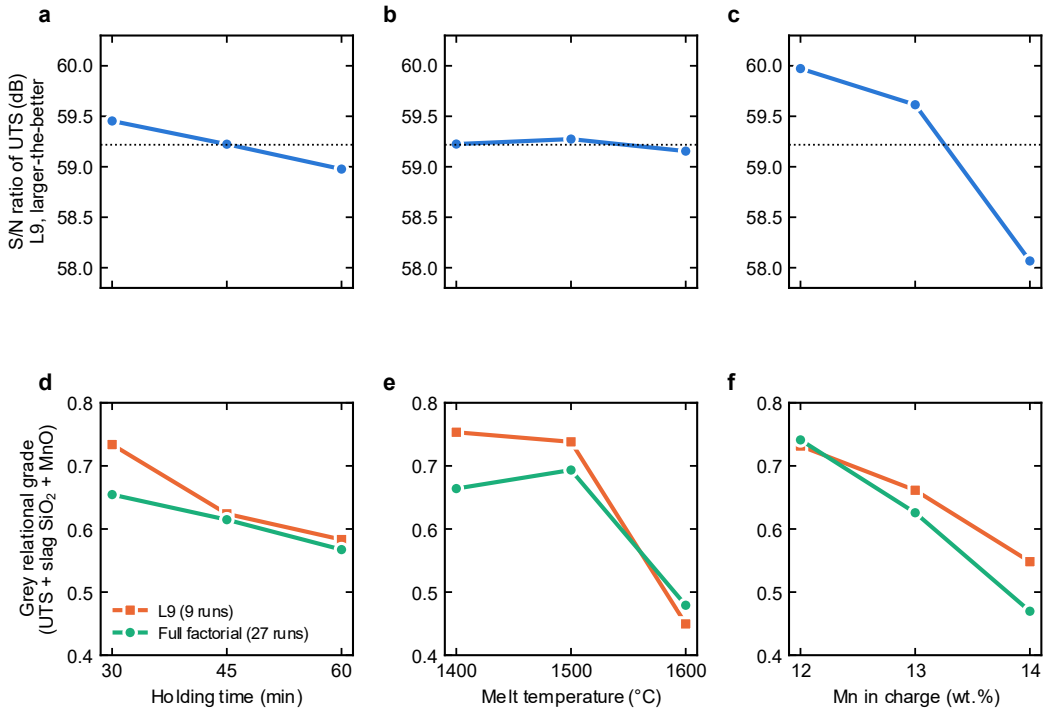


Fig. 9 (a–c) Main effects of the Taguchi L9 S/N ratio for UTS. (d–f) Main effects of the grey relational grade combining UTS, slag SiO_2, and slag MnO, for the L9 subset and for the full factorial. Both point to 30 min, 1500 °C, and 12 wt.% Mn, and both identify 1600 °C as the most damaging lining condition.

3.7 Implications for lining life and foundry practice

Under controlled melting, with the temperature never above 1600 °C, timed holds and frequent deslagging, a silica lining that normally fails after 30–40 Hadfield heats completed 81 heats. At the end of the 81-heat service period, the lining still contained 94 wt.% SiO_2 and retained 40% of the original wall thickness at the worst point (prediction iv). This life was reached even though a third of the heats were deliberately made at 1600 °C, the condition that the slag data identify as the most aggressive (Fig. 5). Since slag SiO_2 at 1600 °C was about twice that at ≤1500 °C, running all heats inside the identified window should extend lining life beyond 81 heats. A dedicated lining service trial at the optimum is needed to quantify this. The economic argument is strong. Basic or neutral linings cost four to six times as much as quartzite [12], whereas the measures identified here — tighter temperature control, shorter holds, frequent deslagging, and Mn at the low end of the grade — cost almost nothing to apply. For a foundry such as TATC, doubling the lining service life roughly halves relining downtime and ramming-mix consumption and lowers the risk of metal penetration to the coil and the associated safety hazard.

Several limitations qualify these conclusions and point to further work. The EDX-XRF analyses were semi-quantitative and covered only SiO_2 and MnO in the slag, so slag basicity and the total mass of slag generated per heat could not be calculated. A full slag analysis and a slag mass balance would allow quantification of silica dissolution in absolute terms. The 81-heat life comes from a single lining service cycle (from installation to relining), and the 30–40-heat baseline comes from plant records rather than from a parallel control lining, so replicate lining service trials are needed to establish the statistical spread of lining life. The deslagging practice and temperature control were changed together, so their separate contributions to the longer lining life cannot be isolated. Finally, the tensile results refer to as-cast, unmachined bars. Solution-treated specimens and SEM/EDS of the lining reaction layer and of the grain-boundary carbides would strengthen the mechanistic interpretation.

4 Conclusions

A 3^3 full-factorial experimental program of 81 heats on a single silica lining in an industrial 500 kg induction furnace showed that different processing factors govern Hadfield steel strength and lining attack. Charge manganese explained 94% of the variation in UTS but only 4% of lining dissolution (slag SiO_2), whereas melt temperature explained 80% of lining dissolution and 61% of manganese oxidation (slag MnO) but less than 0.1% of strength, with long holds harmful mainly at 1600 °C. Melting at 1600 °C therefore doubled silica uptake by the slag without any gain in strength. Using nine of the 27 conditions, the Taguchi L9 analysis correctly ranked the factors and predicted the optimum of 30 min, 1500 °C and 12 wt.% Mn (1027.9 MPa), confirmed by three dedicated heats (1029.9 ± 1.5 MPa) and by the factorial run at 1017 MPa. The same condition gave the lowest slag MnO and ranked first in the multi-response analysis, so the strength optimum is also the lining-protection optimum.

Operating with controlled temperature, timed holding, and frequent deslagging, the lining completed 81 heats, about twice the previous life of 30–40, even though a third of the heats were made at the most aggressive temperature. Confining melting to the window of about 1500 °C, 30–45 min, and 12–13 wt.% Mn is expected to extend lining life further. For foundries that rely on inexpensive acid linings, the practical rule is to set strength through the charge composition and to protect the lining through the thermal schedule. In the future, it is plausible to replicate lining service trials entirely within the window, conduct a full slag mass balance, and characterize the reaction layer with high-resolution electron microscopy.

Acknowledgements

The authors thank TATC–NYUMBU for access to the foundry and induction furnace, and the Tanzania Bureau of Standards for the EDX analyses.

Statements and Declarations

Funding

The authors declare that they received no funds, grants, or other support during the preparation of this manuscript.

Competing interests

The authors have no relevant financial or non-financial interests to disclose.

Author contributions

L.D. Mwakalukwa conducted the investigation, designed and ran the melting program, and wrote the original manuscript. R.J. Katemi conceived the Taguchi, full-factorial, multi-response analyses and ANOVA analysis, reviewed and edited the manuscript, and co-supervised the work. N.E. Mushi supervised the work, participated in the analysis, prepared the figures, and reviewed and edited the final manuscript. All authors read and approved the final manuscript.

Data availability

All data supporting this study are given in Tables 3, 4 and 6 and in the Supplementary Information. The raw spectrometry and tensile records are available from the corresponding author on reasonable request.

References

1. ASTM A128/A128M. Standard specification for steel castings, austenitic manganese. ASTM International, West Conshohocken
2. Subramanyam DK, Swansiger AE, Avery HS (1990) Austenitic manganese steels. In: ASM Handbook, Vol 1, Properties and selection: irons, steels, and high-performance alloys. ASM International, Materials Park, pp 822–840
3. Sabzi M, Farzam M (2019) Hadfield manganese austenitic steel: a review of manufacturing processes and properties. Mater Res Express 6:1065c2
4. Havel D (2017) Austenitic manganese steel: a complete overview. Columbia Steel Casting Co., Portland

5. Gürol U, Kurnaz SC (2020) Effect of carbon and manganese content on the microstructure and mechanical properties of high manganese austenitic steel. J Min Metall Sect B Metall 56:171–182
6. Gürol U, Karadeniz E, Çoban O, Kurnaz SC (2021) Casting properties of ASTM A128 Gr. E1 steel modified with Mn-alloying and titanium ladle treatment. China Foundry 18:199–206
7. Sasaki T, Watanabe K, Nohara K, Ono Y, Kondo N, Sato S (1982) Physical and mechanical properties of high manganese non-magnetic steel and its application to various products for commercial use. Trans Iron Steel Inst Jpn 22:1010–1020
8. Tęcza G (2022) Changes in microstructure and abrasion resistance during Miller test of Hadfield high-manganese cast steel after the formation of vanadium carbides in alloy matrix. Materials 15:1021. https://doi.org/10.3390/ma15031021
9. Rudnev V, Loveless D, Cook RL (2017) Handbook of induction heating, 2nd edn. CRC Press, Boca Raton
10. Lee WE, Zhang S (1999) Melt corrosion of oxide and oxide–carbon refractories. Int Mater Rev 44:77–104
11. Poirier J (2015) A review: influence of refractories on steel quality. Metall Res Technol 112:410
12. Kukartsev VA, Kukartsev VV, Tynchenko VS et al (2023) Study of the influence of the thermal capacity of the lining of acid melting furnaces on their efficiency. Metals 13:337. https://doi.org/10.3390/met13020337
13. Kukartsev VA, Cherepanov AI, Kukartsev VV, Tynchenko VS, Kurashkin SO, Sergienko RB, Tynchenko VV, Bashmur KA (2022) Increasing the efficiency of foundry production by changing the technology of pretreatment with quartzite. Metals 12:1266. https://doi.org/10.3390/met12081266
14. Kukartsev VA, Cherepanov AI, Kukartsev VV, Tynchenko VS, Kurashkin SO, Tynchenko VV, Sergienko RB, Bashmur KA, Boyko AA, Bukhtoyarov VV (2022) Influence of moisture in quartzite on the lining properties and efficiency of industrial-frequency induction crucible furnaces. Metals 12:1515. https://doi.org/10.3390/met12091515
15. Olsen SE, Tangstad M, Lindstad T (2007) Production of manganese ferroalloys. Tapir Academic Press, Trondheim
16. Zuno-Silva J, Bedolla-Jacuinde A, Martínez-Vázquez J, Pérez-Pérez A, Quintero-Azuara T (2014) Laboratory scale study of uncommon degradation of SiO_2 refractories used on induction furnaces. Nova Sci 6(11):113–134
17. Novák V, Řeháčková L, Rosypalová S, Matýsek D (2022) Wetting of refractory ceramics with high-manganese and structural steel and description of interfacial interaction. Crystals 12:1782. https://doi.org/10.3390/cryst12121782
18. von Schweinichen P, Chen Z, Senk D, Lob A (2013) Effect of different casting parameters on the cleanliness of high manganese steel ingots compared to high carbon steel. Metall Mater Trans A 44:5416–5423. https://doi.org/10.1007/s11661-013-1949-7
19. Kong L, Deng Z, Zhu M (2018) Reaction behaviors of Al-killed medium-manganese steel with different refractories. Metall Mater Trans B 49:1444–1452. https://doi.org/10.1007/s11663-018-1223-x
20. Wang L, Zhu H, Zhao J, Song M, Xue Z (2022) Steel/refractory/slag interfacial reaction and its effect on inclusions in high-Mn high-Al steel. Ceram Int 48:1090–1097
21. Sarkar R, Sohn HY (2018) Interactions of alumina-based and magnesia-based refractories with iron melts and slags: a review. Metall Mater Trans B 49:1860–1882
22. Elliott R, Coley K, Mostaghel S, Barati M (2018) Review of manganese processing for production of TRIP/TWIP steels, part 1: current practice and processing fundamentals. JOM 70:680–690
23. Arapov SL, Belyaev SV, Kosovich AA, Partyko EG (2023) An approach to calculating the casting temperature of high-manganese austenite steel. CIS Iron Steel Rev 26:45–50. https://doi.org/10.17580/cisisr.2023.02.07
24. Sabzi M, Moeini Far S, Mersagh Dezfuli S (2018) Effect of melting temperature on microstructural evolutions, behavior and corrosion morphology of Hadfield austenitic manganese steel in the casting process. Int J Miner Metall Mater 25:1431–1438. https://doi.org/10.1007/s12613-018-1697-1
25. Balogun SA, Esezobor DE, Agunsoye JO (2008) Effect of melting temperature on the wear characteristics of austenitic manganese steel. J Miner Mater Charact Eng 7:277–289
26. Taguchi G, Chowdhury S, Wu Y (2005) Taguchi's quality engineering handbook. Wiley, Hoboken

27. Ross PJ (1996) Taguchi techniques for quality engineering, 2nd edn. McGraw-Hill, New York
28. Phadke MS (1989) Quality engineering using robust design. Prentice Hall, Englewood Cliffs
29. Deng JL (1989) Introduction to grey system theory. J Grey Syst 1:1–24
30. Kuo Y, Yang T, Huang GW (2008) The use of grey relational analysis in solving multiple attribute decision-making problems. Comput Ind Eng 55:80–93
31. Muhaba AM (2025) Multi-objective optimization and performance evaluation of rotary furnace refractory linings using locally sourced materials. Adv Mech Eng. https://doi.org/10.1177/16878132251346230
32. Jansson S (2008) A study on the influence of steel, slag or gas on refractory reactions. Doctoral thesis, KTH Royal Institute of Technology, Stockholm
33. ASTM A370. Standard test methods and definitions for mechanical testing of steel products. ASTM International, West Conshohocken
34. ASTM E10. Standard test method for Brinell hardness of metallic materials. ASTM International, West Conshohocken
35. ASTM E1245. Standard practice for determining the inclusion or second-phase constituent content of metals by automatic image analysis. ASTM International, West Conshohocken
36. Belay AS, Tsegaw FG, Gebeyehu SG (2024) Optimization of process parameters using Taguchi and ANOVA. J Eng Ind Res 5(3):152–162
37. Montgomery DC (2017) Design and analysis of experiments, 9th edn. Wiley, Hoboken
38. Mwakalukwa LD (2023) Investigating the process variables affecting melting of manganese steel in a coreless induction furnace constructed with silica lining. MSc (Engineering Materials) thesis, University of Dar es Salaam, Dar es Salaam
39. Allain S, Chateau JP, Bouaziz O, Migot S, Guelton N (2004) Correlations between the calculated stacking fault energy and the plasticity mechanisms in Fe–Mn–C alloys. Mater Sci Eng A 387–389:158–162
40. Saeed-Akbari A, Imlau J, Prahl U, Bleck W (2009) Derivation and variation in composition-dependent stacking fault energy maps based on subregular solution model in high-manganese steels. Metall Mater Trans A 40:3076–3090

Supplementary Files

This is a list of supplementary files associated with this preprint. Click to download.

- Supportinginformation12102026.docx